PUBLISHED VERSION

Corbett, Kerry Anne; Hamilton, Murray Wayne
Comparison of the bifurcation scenarios predicted by the single-mode and multimode semiconductor laser rate equations Physical Review E, 2000; 62(5):6487-6495

©2011 American Physical Society

http://link.aps.org/doi/10.1103/PhysRevE.62.6487

PERMISSIONS

http://publish.aps.org/authors/transfer-of-copyright-agreement

"The author(s), and in the case of a Work Made For Hire, as defined in the U.S. Copyright Act, 17 U.S.C.

§101, the employer named [below], shall have the following rights (the "Author Rights"):

[...]

3. The right to use all or part of the Article, including the APS-prepared version without revision or modification, on the author(s)' web home page or employer's website and to make copies of all or part of the Article, including the APS-prepared version without revision or modification, for the author(s)' and/or the employer's use for educational or research purposes."

24th April 2013

http://hdl.handle.net/2440/12765

Comparison of the bifurcation scenarios predicted by the single-mode and multimode semiconductor laser rate equations

K. A. Corbett and M. W. Hamilton
Department of Physics and Mathematical Physics, University of Adelaide, Adelaide, South Australia, 5005, Australia
(Received 2 June 2000)

We present a detailed comparison of the bifurcation scenarios predicted by single-mode and multimode semiconductor laser rate equation models under large amplitude injection current modulation. The influence of the gain model on the predicted dynamics is investigated. Calculations of the dependence of the time averaged longitudinal mode intensities on modulation frequency are compared with experiments performed on an $Al_xGa_{1-x}As$ Fabry-Pérot semiconductor laser.

PACS number(s): 05.45.−a

I. INTRODUCTION

Direct current modulation of semiconductors lasers has applications in optical fiber communication systems [1] and short pulse generation [2]. Due to the inherently nonlinear nature of these devices, the dynamical variation of the photon and carrier densities exhibit complicated behavior. A knowledge and understanding of this behavior is essential for the implementation of these devices in practical applications. The study of semiconductor lasers is also of interest from the nonlinear dynamics viewpoint, and the wide variety of dynamical behaviors exhibited by these devices under different operating conditions has received much attention in recent years [1–32].

As a physical system the semiconductor laser involves the interaction of the electromagnetic field with the electron and hole populations of an inverted semiconductor crystal; as such it is a nonequilibrium, many-body system, and is very difficult to model from first principles. However, by the application of several simplifying assumptions, the dynamical equations for the individual carriers and photons can be reduced to a set of rate equations describing the evolution of the total carrier and photon densities in the active region [33]. Nevertheless, it is important to realize that these equations represent a considerable approximation to the actual semiconductor laser system, a fact that has led to a diversity of models proposed to describe their operation. In this paper we compare the bifurcation behavior under sinusoidal modulation predicted by several frequently used rate equation models applicable to Fabry-Pérot (FP) lasers. Emphasis is placed on the implications that inclusion of multiple longitudinal modes and choice of gain model have on the predicted dynamics. We also make comparisons with experiments performed on $Al_xGa_{1-x}As$ FP semiconductor lasers.

The nonlinear behavior of semiconductor laser devices under current modulation has been principally modeled using single-mode rate equations. These equations predict a rich variety of behaviors such as period doubling routes to chaos, period tripling, multiple spiking, and hysteresis [16–29]. However, not all these behaviors are observed experimentally. Only period doubling [16,17,21,29] and multiple spiking [16,17] have been observed in current modulated FP lasers, whereas in distributed feedback (DFB) lasers period doubling [24,29,30], period tripling [29,30], and chaos [30] have been observed. The discrepancy between single-mode rate equation predictions and experimental observations has been attributed to damping of the relaxation oscillations caused by gain saturation [14,15], and the spontaneous emission parameter [26,29].

In contrast there are very few studies of the dynamics predicted by the multimode rate equations. To the best of our knowledge, a study of the bifurcation scenarios occurring with a change in the modulation frequency and amplitude has not been attempted, though there have been studies on the transient behavior [3,4,7] and spectral characteristics [2,8–11]. That FP lasers become multimode under injection current modulation is well known [8–10]. However, as shown by Tarucha and Otsuka [2], this is dependent not only upon the amplitude but also the frequency of the modulation; modulating at frequencies close to the relaxation oscillation frequency leads to a significant increase in the number of longitudinal modes, with the spectrum shifting toward shorter wavelength modes. This effect was shown to result from the spectral shift of the gain with carrier density; an increase in the carrier density results in the population of higher energy states (referred to as band filling [33,2]), and thus gives rise to a spectral shift of the gain. Since injection current modulation results in dynamical carrier density variation, it is reasonable to expect the above consideration to affect the bifurcation phenomena as well as spectral behavior under large amplitude current modulation. Despite this, there were very few studies of the bifurcation behavior, with injection current modulation, which include the effects of band filling [2].

The purpose of this paper is to compare the bifurcation behavior for single-mode and multimode models (with and without band filling) with experimental measurements of the dependence of the time averaged longitudinal mode intensities on modulation frequency, to demonstrate that the multimode model with band filling provides the most accurate description of FP semiconductor laser operation. This paper is organized as follows. The rate equations are introduced in Sec. II. In Sec. III, numerical results for the both single-mode and multimode rate equations are presented, using typical literature values for the laser parameters. Bifurcation diagrams, the time averaged longitudinal mode intensities versus modulation frequency, and the global behavior in the

 ©2000 The American Physical Society

modulation frequency and amplitude parameter space are discussed. In Sec. IV, experimental results of the time averaged longitudinal mode intensities versus modulation frequency are presented and compared with the numerical predictions of the multimode rate equations using experimentally determined parameter values. Experimental results for period doubling are also presented. Finally, concluding remarks are made in Sec. V.

II. RATE EQUATIONS

The multimode rate equations for the carrier density n and the longitudinal mode photon densities s_j and phases Φ_j in the active region of a semiconductor laser can be written as [2,10,32]

$$\frac{dn}{dt}=\frac{I(t)}{eV}-\frac{n}{\tau_e}-\sum_{j=-(M-1)/2}^{(M-1)/2}G_j s_j, \tag{2.1}$$

$$\frac{ds_j}{dt}=\left(G_j-\frac{1}{\tau_p}\right)s_j+\frac{\beta_j n}{\tau_e}, \tag{2.2}$$

$$\frac{d\Phi_j}{dt}=\frac{\alpha}{2}\left(G_j-\frac{1}{\tau_p}\right) \tag{2.3}$$

where e is the electronic charge, V is the active region volume, τ_e and τ_p are the carrier and photon lifetimes, respectively, α is the linewidth enhancement factor, G_j is the gain of the jth mode, and M is the total number of modes. Under sinusoidal modulation the injection current has the form $I(t)=I_{DC}+I_{AC}\sin(2\pi ft)$ where f is the modulation frequency. These equations are appropriate for a FP semiconductor laser, and assume single transverse mode operation.

The parameter β_j is the fraction of the total average spontaneous emission coupled into the jth mode. It contains two parts: a geometrical factor, given by the ratio of the mode solid angle to 4π, and a spectral component resulting from the fact that the spontaneous emission spectrum is much broader than the mode spectral width [34,35]. To a very good approximation, the geometrical factor is the same for all longitudinal modes whereas the spectral component will vary slightly for different modes since they lie in different regions of the spontaneous emission spectrum. However, for modes lying near the gain peak the variation in β between different longitudinal modes is small. Since it is principally these modes that participate in the dynamics, we make the simplifying approximation $\beta_j=\beta$.

The semiconductor gain is assumed to saturate homogeneously, and is approximated by a quadratic for which both the peak gain and its position in wavelength are linear functions of the carrier density [2]. These approximations are consistent with the predictions of the free carrier theory [33]. We write the gain G_j as [2,13,36]

$$G_j=An\left[1-\left\{\frac{2(\lambda(n)-\lambda_j)}{\Delta\lambda_g}\right\}^2\right]-An_o, \tag{2.4}$$

$$\lambda(n)=\lambda_o+k\left[\frac{n_{th}-n}{n_{th}}\right], \tag{2.5}$$

where j runs from $-(M-1)/2$ to $(M-1)/2$. The constants n_{th} and n_o are, respectively, the threshold carrier density and the carrier density required to reach transparency, A is the gain coefficient, $\Delta\lambda_g$ is the spectral width of the gain, and $\lambda(n)$ is the center wavelength of the spectral gain curve. The constant k defines the spectral shift of the gain with carrier density due to the band-filling effect. The longitudinal mode wavelengths λ_j are given by

$$\lambda_j=\lambda_o+j\,\delta\lambda+\delta\Lambda_j, \tag{2.6}$$

where $\delta\lambda=\lambda_o^2/(2L)$ is the approximate longitudinal mode spacing. Here L is the optical length of the diode cavity. The quantity $\delta\Lambda_j$ describes the time variation of the modal wavelengths arising as a consequence of Eq. (2.3), and is written as

$$\delta\Lambda_j=-\frac{1}{2\pi}\left(\frac{d\Phi_j}{dt}\right)\frac{(\lambda_o+j\,\delta\lambda)^2}{c}. \tag{2.7}$$

For numerical purposes it is convenient to normalize the variables n and s_j by defining $N=n/n_{th}$ and $P_j=s_j/\tilde{s}_0$ where $n_{th}=n_o+1/A\tau_p$ is the threshold carrier density and $\tilde{s}_0=n_{th}\tau_p/\tau_e$ [23]. Equations (2.1), (2.2), and (2.3) become

$$\frac{dN}{dt}=\frac{1}{\tau_e}\left[I'(t)-N-\sum_{j=-(M-1)/2}^{(M-1)/2}\frac{N\delta_j-\delta}{1-\delta}P_j\right], \tag{2.8}$$

$$\frac{dP_j}{dt}=\frac{1}{\tau_p}\left[\left(\frac{N\delta_j-\delta}{1-\delta}\right)P_j-P_j+\beta N\right], \tag{2.9}$$

$$\frac{d\Phi_j}{dt}=\frac{\alpha}{2\tau_p}\left[\frac{N\delta_j-\delta}{1-\delta}\right], \tag{2.10}$$

where $\delta=n_o/n_{th}$, $I'(t)=I(t)/I_{th}$, and $I_{th}=eVn_{th}/\tau_e$ is the threshold current. We also define the quantities $I_b=I_{DC}/I_{th}$ and $m=I_{AC}/I_{th}$ which will be referred to as the modulation index. The gain spectral dependence is embodied by

$$\delta_j=1-4\left(\frac{k(1-N)-j\,\delta\lambda-\delta\Lambda_j}{\Delta\lambda_g}\right)^2. \tag{2.11}$$

In Sec. III, comparisons will be made between the solutions of the single-mode rate equations with those of the multimode rate equations. In single-mode models, a frequently used approximation for the gain versus carrier density is

$$G=A(n-n_o), \tag{2.12}$$

which we employ in all single-mode calculations presented here. The single-mode rate equations may be obtained from Eqs. (2.8) and (2.9) by setting the band-filling parameter $k=0$ (i.e., neglect band filling) and considering only the central mode, λ_0; this leads to the rate equations used in Refs. [14–21,23] except for the omission of the gain saturation term. The phase equation (2.10) is not used in the single-mode analysis presented here in order to retain consistency with previous studies.

We have not considered the effects of gain saturation in this study, though we acknowledge their importance. Since we are concerned with the dynamical variations of the modal

TABLE I. Parameter values for the rate equations.

Symbol	Sec. III	Sec. IV	Model
τ_e	3 ns	0.78 ± 0.05 ns	both
τ_p	6 ps	2.2 ± 0.1 ps	both
δ	0.692	0.15 ± 0.07	both
β	10^{-4}	2×10^{-5}	both
α	5	5	both
$\Delta\lambda_g$	20 nm	30 nm	multimode
$\delta\lambda$	0.4 nm	0.37 ± 0.02 nm	multimode
k	35 nm	19 ± 3 nm	multimode
λ_o	830 nm	837 ± 4 nm	multimode
M	25	25	multimode

photon densities, rather than the steady state operation of semiconductor laser devices, the inclusion of gain saturation leads to a significant increase in the complexity of the problem. Analysis of gain saturation effects requires taking into account dynamical changes in the gain spectra, such as spectral hole burning, with variation in the longitudinal intensities [1]. Since such variations imply a departure from quasiequilibrium, the dynamics of the individual carriers must be considered rather than the dynamics of the carrier density as a whole [33]; this leads to a rapid escalation in the computing time required to analyze this problem. So, for simplicity, such effects have been omitted.

Parameter values used in numerical calculations are given in Table I. The first column, labeled ''Sec. III,'' contains the parameter values used in the numerical simulations of Sec. III. These are typical literature values for an $Al_xGa_{1-x}As$ semiconductor laser. For the sake of comparison with existing studies, parameter values which apply to both the single mode and multimode are identical to those used in Refs. [14,19,22,23]. The column labeled ''Sec. IV'' in Table I contains our experimentally measured parameter values. In Sec. IV these parameter values are used for comparison between experimental data and the numerical predictions of Eqs. (2.8)–(2.10). A discussion of the measurements used to obtain these parameter values is given in Sec. IV.

For small perturbations from the steady state, the rate equations predict behavior similar to that of a linear oscillator with a characteristic resonant frequency f_{RO} referred to as the relaxation oscillation frequency. To a good approximation, f_{RO} is given by [3,23]

$$f_{RO}=\frac{1}{2\pi}\sqrt{\frac{I_b-1}{\tau_e\tau_p(1-\delta)}} \tag{2.13}$$

for both the single-mode and multimode models. With large amplitude modulation, Eq. (2.13) no longer applies [23,26]. However, f_{RO} is a useful quantity when searching for the various transitions in the (f,m) parameter space [27,37].

III. NUMERICAL RESULTS

In this section, the results of numerical simulations of Eqs. (2.8)–(2.10) are presented. The value $I_b=1.7$ is used in all calculations, and corresponds to a small signal relaxation oscillation frequency of 1.788 GHz. The other parameter values are given in the column labeled ''Sec. III'' in Table I. For the single-mode system, the parameters k and M are set to 0 and 1, respectively.

A. Comparative study of bifurcations

In the following, the solutions for the single-mode and multimode rate equations, with and without band filling, are compared. Results are presented in the form of bifurcation diagrams, obtained by stroboscopically sampling the variables at the period of the driving current $T=1/f$ as a control parameter, usually modulation index or frequency, is varied. Diagrams are calculated for both increasing and decreasing values of the control parameter. For the sake of comparison, bifurcation diagrams of the variable N are presented for both the single-mode and multimode cases.

In Fig. 1 we present bifurcation diagrams calculated with varying modulation frequency, f. Figures 1(a) and 1(b) correspond to single-mode calculations with modulation indices of 0.5 and 0.75 respectively; Figs. 1(c) and 1(d) are the corresponding multimode calculations for the same modulation indices.

We observe marked differences in the bifurcation scenarios predicted in each case. As shown in previous studies, both a period doubling cascade to chaos [18,19,22] and regions of hysteresis (HS_1 and HS_2) [18,26] are predicted by the single-mode rate equations [Figs. 1(a) and 1(b)]. Both these features are absent in the multimode system [Figs. 1(c) and 1(d)] under similar operating conditions. However, both single-mode and multimode rate equations predict period doubling to occur for modulation frequencies near $2f_{RO}$.

The differences between the predicted behavior for the single-mode and multimode models, shown in Figs. 1(a)–1(d), are the result of both the inclusion of multiple longitudinal modes and the nonzero value of the band-filling parameter k. In order to illustrate this point, Figs. 1(e) and 1(f) show bifurcation diagrams for the same parameter values as in Figs. 1(c) and 1(d), but with the band-filling parameter k equal to zero. We remark that $k=0$ is consistent with the gain model used in Refs. [7–13,1]. However, Refs. [7–9] used a Lorentzian rather than a quadratic approximation for the gain curve. The results of the multimode calculation without band-filling resemble the single mode solutions [Figs. 1(a) and 1(b)] more closely than the multimode solutions with band-filling [Figs. 1(c) and 1(d)]. Figures 1(a) and 1(e) are similar except that the period doubling region is narrower in Fig. 1(e) and only the hysteresis region HS_1 occurs. In Fig. 1(f), we observe that the period doubling cascade to chaos and the hysteresis region, HS_2 of Fig. 1(b), is absent but the period doubling regions near $f_{RO}/2$ and $2f_{RO}$ and hysteresis region HS_1 persist. Therefore, the behavior shown in Figs. 1(e) and 1(f) lies somewhere between that depicted in Figs. 1(a) and 1(b) and 1(c) and 1(d). This highlights the fact that the dynamical behavior is sensitive to the choice of gain function used.

It is evident from Fig. 1 that the inclusion of multiple longitudinal modes acts to reduce the number of bifurcations that occur. Multiple longitudinal mode oscillation results in an increased damping of the relaxation oscillations, as demonstrated in Refs. [8,10,13]. Since the relaxation oscillation resonance is intimately connected with the occurrence of bifurcations [38,37], the larger the damping the more difficult

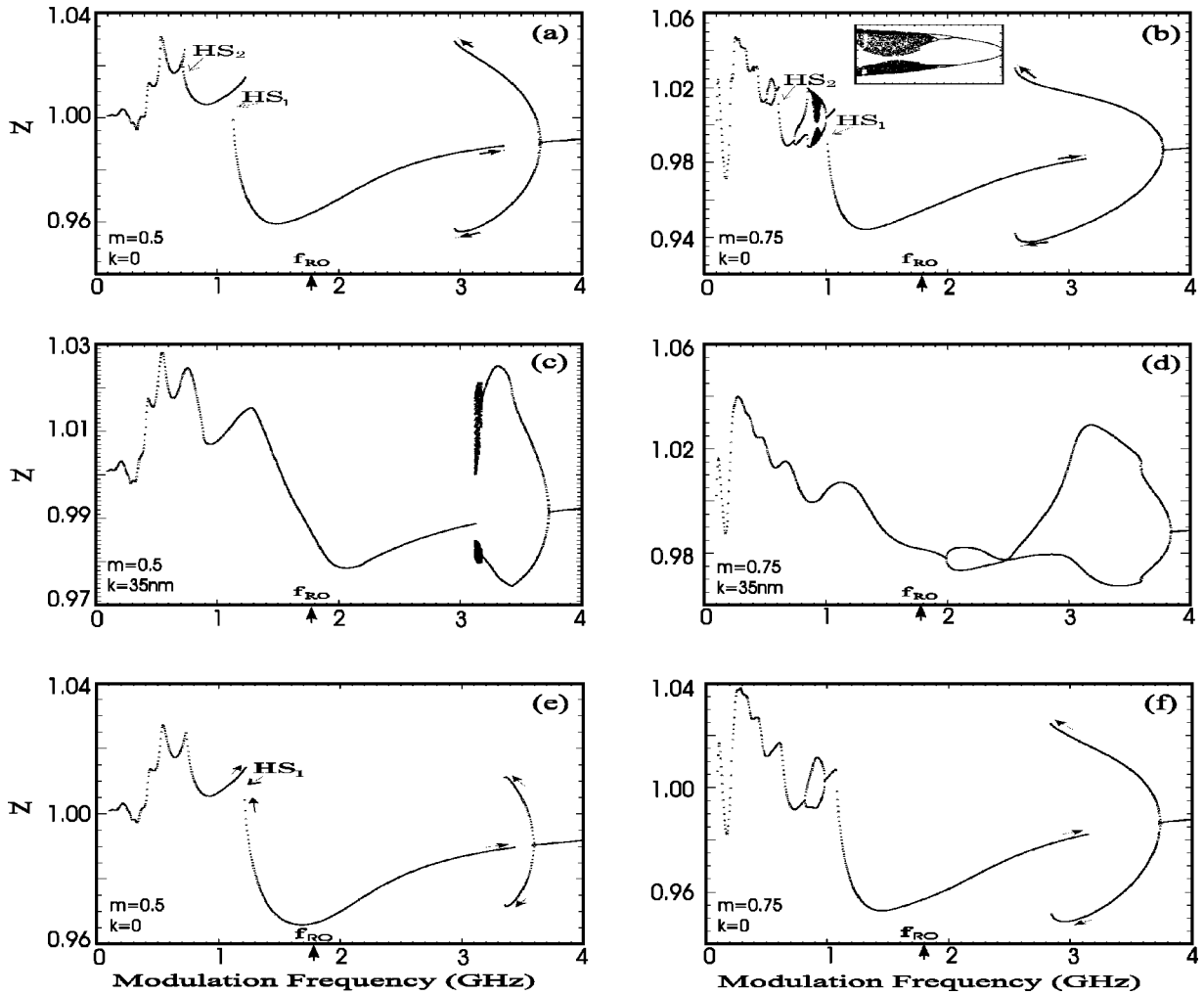

FIG. 1. Bifurcation diagram: parts (a) and (b) correspond to the single-mode equations for modulation indices of $m=0.5$ and 0.75, respectively. An expanded view of the period doubling cascade to chaos is shown in the inset in (b). Parts (c) and (d) are the diagrams for the multimode system for $m=0.5$ and 0.75, respectively, and $k=35$ nm. Parts (e) and (f) are the diagrams for the multimode system for $m=0.5$ and 0.75, respectively, and $k=0$. *HS* refers to regions of hysteresis.

it is to drive the system to an instability. In Refs. [14,16] it was postulated that instabilities would only occur if the decay time of the relaxation oscillations exceeded the modulation period, since in this case strong interferences occur between successive periods. The disparity between the nonlinear behavior predicted by the single-mode equations and experimental observations received much attention in the literature. It was previously demonstrated that damping terms in the rate equations due to the parameter β will reduce the nonlinear behavior [10,13,26,29]. Other physical causes of damping in semiconductor lasers are gain compression [14,15], carrier diffusion [9,13], and carrier density dependent spontaneous lifetime [31]. It was also shown that the presence of intrinsic laser noise acts to obscure higher order period doublings in experiments [21]. Our calculations show that for FP lasers, the multimode nature of the device under modulation also plays a role in suppressing higher order period doubling and other nonlinear behavior, consistent with experimental observations.

The inclusion of band-filling effects clearly alters the dynamical behavior, as shown in Fig. 1. This may be understood through consideration of the gain each mode experiences as the carrier density is varied. Equations (2.4) and (2.5) show that the inclusion of band filling ($k\neq 0$) leads to a quadratic dependence of the modal gain on carrier density, whereas when band-filling is neglected ($k=0$) the dependence is linear. Since the value of k is usually of the order of the gain width and much larger than the longitudinal mode spacing, band-filling effects lead to a significant shift in the gain peak even for moderate modulation depths. This results in different modes being closest to the gain peak over the course of a modulation period, and therefore this phenomena is extremely important in the dynamical description of these devices.

B. Modal behavior

In terms of the bifurcation behavior, the bifurcation diagrams for each longitudinal mode show qualitatively similar behavior to those for the carrier density, and are omitted here. It is illustrative to consider, however, how the time averaged modal photon densities vary as the modulation frequency is tuned. To calculate the time averaged photon densities for a periodic solution, we average the modal photon densities over the period of the cycle. In order to be able to summarize this data on a three-dimensional plot, we multiply

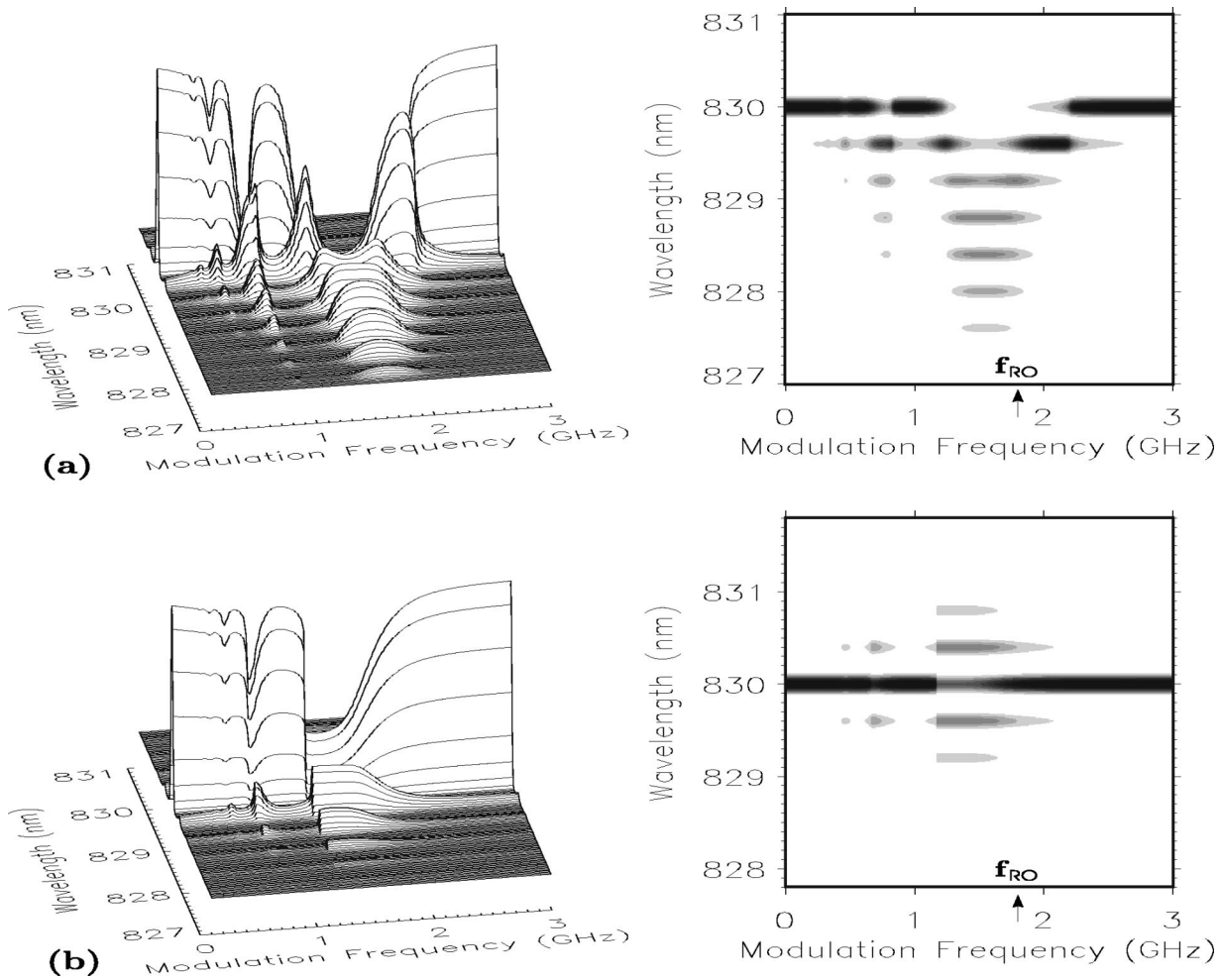

FIG. 2. The time averaged longitudinal mode spectra as a function of modulation frequency with $m=0.5$. Data plotted as surface and grayscale plots. In these the darkest gray corresponds to the maximum intensity. In parts (a) and (b) $k=35$ nm and 0, respectively.

the photon density for each longitudinal mode by the (Lorentzian) spectral resolution function of the spectrometer used in the experiments presented in Sec. IV; this also facilitates comparisons with the experimental data.

Figure 2(a) shows the time averaged longitudinal mode photon density variation with modulation frequency for the same parameters as Fig. 1(c). For modulation frequencies near f_{RO} the spectrum becomes strongly multimode with the spectrum shifting toward the shorter wavelength modes; this phenomenon has been predicted theoretically, and observed experimentally [2]. We also observe multimode operation when the higher harmonics of f are near f_{RO}; most notable are the regions near $f\approx 0.85$ and 0.55 GHz which correspond to the second and third harmonic of the driving frequency near f_{RO}, respectively. Figure 2(b) corresponds to the same situation as Fig. 2(a), except the band-filling parameter k is zero. Modal photon densities are calculated for increasing modulation frequency only; hence the hysteresis region of Fig. 1(e) is not apparent. Again we observe multimode behavior for modulation frequencies near f_{RO}, $f_{RO}/2$, $f_{RO}/3$, etc. However, now the spectra are symmetric about the central mode.

At a resonance, the excursion of the carrier density from its steady state value is largest. This gives rise to strongly multimode oscillation as shown in Fig. 2. The obvious asymmetry in Fig. 2(a) is a result of band-filling effects. We remark that the dynamical spectral behavior under modulation is also dependent upon the modulation amplitude [8]. Separate calculations show that the number of oscillating modes is reduced for lower modulation indices, when the modulation frequency (or a harmonic) is close to f_{RO}. For higher modulation indices, the number of oscillating modes increases even for modulation frequencies not close to a resonance; thus the frequency dependence of the modulation behavior is not as readily resolved as in the case considered here.

C. Global behavior

To summarize the global behaviors, in Fig. 3 the transition boundaries between period 1 and 2 and period 2 and 4 solutions are plotted as functions of the modulation index and frequency on a two-dimensional state diagram. We also show the boundaries for Hopf bifurcations. The data in Fig. 3 were calculated numerically by checking for period 1 and 2 solutions of the rate equations for a square grid of modulation frequencies and amplitudes. Regions of hysteresis between period 1 cycles are not shown, as they could not be determined using our method of calculation; however, re-

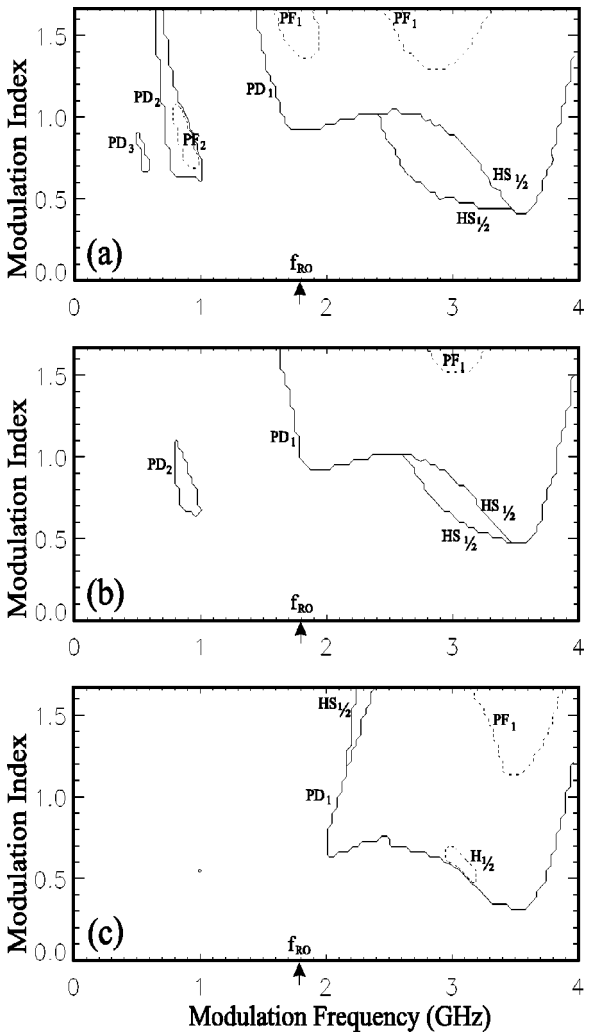

FIG. 3. Period doubling and Hopf bifurcation boundaries in the parameter space of modulation frequency and modulation index. Part (a) is for the single mode model, and parts (b) and (c) are for the multimode model with $k=0$ and 35 nm, respectively. The solid lines labeled by *PD* indicate boundaries between period-1 and -2 solutions. Solid lines labeled by *HS* indicate the boundaries between period -1 and -2 solutions in which hysteresis is involved. Dashed lines labeled by *PF* indicate the boundaries between period -2 and -4 solutions, and dashed lines labeled by *H* indicate boundaries for Hopf bifurcations.

gions of hysteresis between period 1 and 2 solutions are included. The resolution of these diagrams is 0.032 in *m* and 0.038 GHz in *f*.

In Fig. 3(a) we present the single-mode solutions. This figure is similar to that shown in Ref. [22] for $I_b=1.5$. We observe regions of period doubling that become smaller and more closely spaced as the modulation frequency decreases. This behavior is typical of many nonlinear oscillators [39]. The period 4 region near $f\approx 1$ GHz contains chaotic solutions [compare with Fig. 1(b)]. Figure 3(b) shows multimode solutions without band-filling effects. This diagram is similar to the single-mode case except that period doubling regions are smaller and only two are present. There are no period 4 (or higher) solutions, for $f<f_{RO}$, in this case. Figure 3(c) shows the multimode solutions, including band-filling effects. The large region of period doubling for $f>f_{RO}$ (which includes the boundaries for bifurcation to period 4 and Hopf bifurcations) is present. However, there is no period doubling for modulation frequencies less than the relaxation oscillation frequency in this case. It is interesting to note that the minimum modulation index required for period doubling, which occurs for modulation frequencies close to $2f_{RO}$, is lower in the multimode system with band filling than the other models.

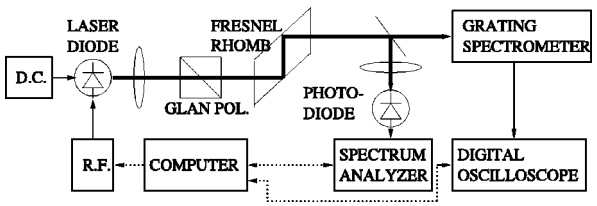

FIG. 4. The experimental arrangement.

IV. EXPERIMENTAL RESULTS

In this section, a comparison of the results of experiments performed on an $Al_xGa_{1-x}As$ semiconductor laser with the numerical predictions of the multimode model with band filling is presented. Before discussing the experimental results, we first describe the measurements used for the experimental determination of the laser parameters. The values obtained from these measurements are summarized in the column labeled ''Sec. IV'' in Table I, and are used in all numerical calculations discussed in this section.

A. Laser parameters

The experimental arrangement, shown in Fig. 4, allows measurement of the power spectrum of the total intensity and the longitudinal mode spectra. A Fabry-Perot laser with an $Al_xGa_{1-x}As$ active region (wavelength approximately 830 nm, maximum power 5 mW) was used in the experiment. The combination of a Glan-type polarizer and a Fresnel rhomb was used to isolate the laser from back reflections. The temperature of the laser was stabilized to 25 °C using a Peltier cell and a temperature control unit. The threshold current at this temperature is 21 mA.

The power spectrum of the total intensity was measured by focusing the laser output into a photodiode (bandwidth 6 GHz) connected to a spectrum analyzer. Time averaged longitudinal mode spectra were measured using a grating spectrometer with a linear photodiode array in place of the exit slit. The output of the spectrometer was connected to a digital oscilloscope. Injection current modulation at frequencies up to 3 GHz was provided by a rf signal generator.

The majority of the parameter values were determined from the measurement of the gain spectra, according to the method of Hakki and Paoli [40], for several different bias currents below threshold. The longitudinal mode spacing $\delta\lambda$ was determined directly from the emission spectrum of the laser biased below threshold. To determine the remaining parameters, the total cavity loss α_c, which includes mirror losses, is required. This was determined from the gain spectra measurements using the following observations: at the threshold current the gain equals the loss and therefore the peak gain is zero, whereas for wavelengths just below the

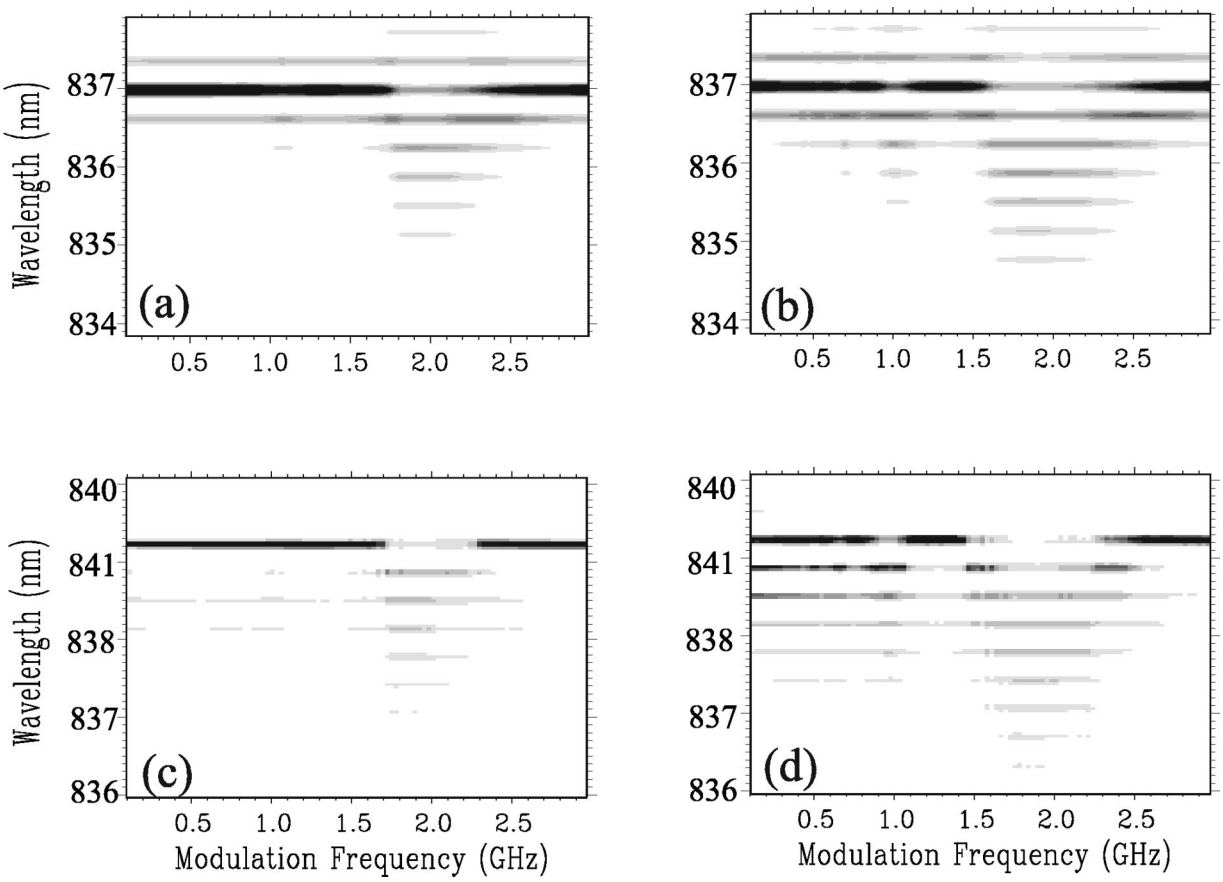

FIG. 5. The longitudinal mode spectra vs modulation frequency for modulation indices of 0.17 [parts (a) and (c)] and 0.25 [parts (b) and (d)]. Parts (a) and (b) correspond to the numerical simulations, and parts (c) and (d) are the experimentally measured spectra.

band gap (the transparency region) the semiconductor medium contributes neither net gain or loss. Thus the difference in these levels corresponds to the total cavity loss α_c. The parameter δ was determined from a plot of the peak gain versus injection current. It is given by I_o/I_{th} where I_o is the injection current for which the peak gain equals α_c. The photon lifetime τ_p is determined from

$$\tau_p = \frac{nL}{c\alpha_c L} = \frac{\lambda_o^2}{2\delta\lambda\alpha_c L}, \tag{4.1}$$

where L is the cavity length and n is the refractive index [41]. A plot of the wavelength of the maximum gain versus injection current allows us to determine k according to Eq. (2.5). Finally, by fitting a quadratic to the gain curve for the laser biased at the threshold current, the gain width $\Delta\lambda_g$ and position λ_0 were determined.

The carrier lifetime, τ_e, was determined by measuring the frequency response of the laser biased below threshold [42]. The threshold current I_{th} was determined from the point of inflection of the measured power versus injection current curve plotted on a log-log plot. To determine β, we compared the measured power with the predicted power in the highest power mode versus injection current above threshold. The predicted mode power was calculated using the experimentally determined parameter values, from steady state solutions of Eqs. (2.8) and (2.9), for different values of β. The mode powers, in both experimental and theoretical data, were normalized such that the total power was equal to 1 when the laser was biased at twice the threshold current. A value of $\beta = 2\times10^{-5}$ gave the closest agreement to the experimental data.

We have not measured the value of α but instead use a typical value of $\alpha = 5$ [43]. However, we note that setting $\alpha = 0$ does not significantly alter the results of the calculations presented in this paper for the carrier and photon densities and the time averaged longitudinal mode frequencies. It does, however, affect the instantaneous mode frequencies, and is essential for the description of semiconductor lasers in the presence of external feedback [32].

B. Modal behavior

Figures 5(a) and 5(b) show the predicted longitudinal mode spectra versus modulation frequency for modulation indices of 0.17 and 0.25, respectively, and a fixed bias of $I_b = 1.31$. Figures 5(c) and 5(d) show the corresponding experimentally measured longitudinal mode spectra versus modulation frequency for the same modulation indices and $I_b = 1.31$. The numerical results were obtained using the method outlined in Sec. III B. The experimental results were obtained by recording time averaged longitudinal mode spectra as the modulation frequency is varied in steps of 0.03 GHz from 0.1 to 3.0 GHz. The injection current was 27.5 mA.

Figure 5 shows good agreement between the numerical simulations and experiment. Despite differences in the relative intensities between different longitudinal modes, shown

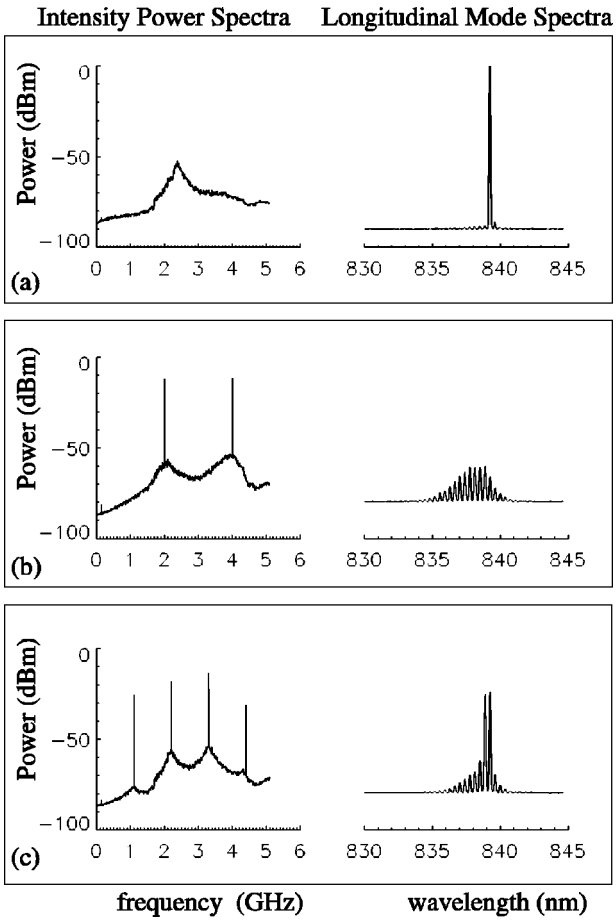

FIG. 6. Experimental intensity power spectra and corresponding time averaged longitudinal mode spectra. Part (a) corresponds to the laser without modulation, part (b) corresponds to modulation at the relaxation oscillation frequency for modulation frequency $f=2$ GHz, and part (c) corresponds to modulation at half the relaxation oscillation frequency for modulation frequency $f=1.1$ GHz. The laser bias is $I_{DC}=27$ mA, and the ac modulation is 4.5 mA (rms).

in the experimental and numerical data of Fig. 5, the general form of the longitudinal mode behavior in each case is similar. In particular, the widths and positions of the multimode regions as a function of the modulation frequency are consistent. Moreover, the multimode regions generally have approximately the same number of longitudinal modes in both the numerical and experimental data.

To demonstrate that the multimode behavior is indeed a resonance phenomenon, we have included the experimental power spectra of the total intensity and the corresponding time averaged longitudinal mode spectra for f near f_{RO} and $2f$ near f_{RO} (Fig. 6). For comparison, we also show the longitudinal mode spectrum and the intensity power spectrum without modulation. We observe, in Figs. 6(b) and 6(c), that the relaxation oscillation resonance has shifted to a lower frequency relative to the unmodulated laser resonance. This phenomena is also observed in numerical simulations: regions of multimode operation are accompanied by frequency pulling of the relaxation oscillations, indicating that this is essentially a nonlinear phenomena.

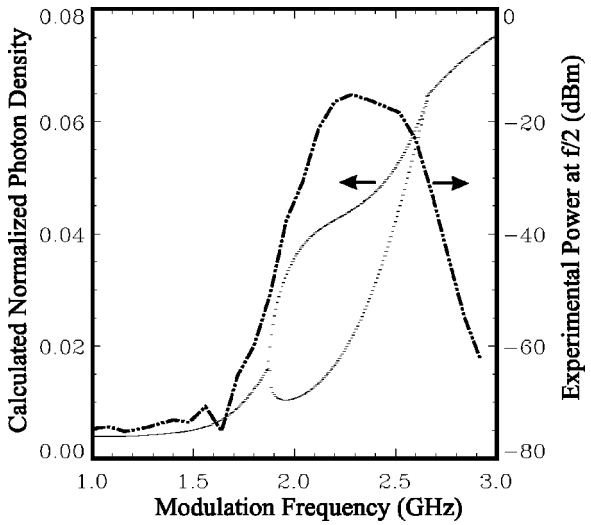

FIG. 7. Period doubling as a function of the modulation frequency for the parameters $I_b=1.095$ and $m=0.28$. The dot-dashed line corresponds to the experimental data, and depicts the measured power at half the modulation frequency in the intensity power spectrum. The dotted curve is a calculated bifurcation diagram showing a period doubling bifurcation.

C. Period doubling

Figure 7 shows a comparison of the experimental data and numerical prediction for the occurrence of period doubling as a function of the modulation frequency for a bias of $I_b=1.095$ and modulation index $m=0.28$. Experimental determination of the occurrence of period doubling is accomplished by measuring the rf power, in the intensity power spectrum, at a frequency equal to half the modulation frequency. Numerically the occurrence of period doubling is demonstrated by means of a bifurcation diagram calculated using the method described in Sec. III A. Data in Fig. 7 are shown for modulation frequencies in the range 1–3 GHz. However, it has been confirmed separately that no further bifurcation occur either experimentally or are predicted numerically for modulation frequencies below 1 GHz.

Figure 7 shows good agreement between theory and experiment. Experimentally the period doubling region appears wider than the numerical prediction. However, it should be noted that a precise determination of the onset of a period doubling bifurcation is difficult to determine experimentally due the presence of noise in the real laser. This arises from the fact that, close to period doubling, there is an enhancement of the noise at $f/2$ which acts to obscure the actual bifurcation point [23,38].

V. DISCUSSION

In this paper we have presented a comparative study of the bifurcation scenarios under sinusoidal current modulation predicted by several rate equation models of varying complexity. Considerable variation in the predicted behavior was found to occur for different models. Due to the complicated nature of the semiconductor system, any description will represent, of necessity, a significant approximation to the actual device.

It was shown that the inclusion of multiple modes acts to reduce the extent of the bifurcation phenomena. Such predic-

tions are consistent with the bifurcations (or lack thereof) observed experimentally in FP semiconductor lasers. The importance of band filling was also investigated. It was shown that the inclusion of band filling results in changes in both the bifurcation behavior predictions and the time averaged longitudinal mode behavior. Moreover, the predictions of the multimode model with band-filling are most closely in agreement with experiment. A distinguishing feature of the experiments was that when a harmonic of the driving frequency, was coincident with the relaxation oscillation frequency an increase in the number of operating modes occurred. Such behavior was predicted by both multimode models investigated. However, the inclusion of band filling led to a spectral shift of the mode spectra toward shorter wavelengths, in agreement with experimental observations, thus demonstrating the importance of this effect.

Despite the simplicity of the multimode rate equation model used in the simulations, good agreement was obtained between the numerical simulations and experimental results. In particular, gain saturation effects were neglected in the model. Though known to have important consequences for the behavior of semiconductor laser devices, we appeal to the consistency of our experimental data and numerical predictions, that the neglect of these effects was not serious for the particular experiments considered in this study. However, in a consistent multimode description the inclusion of gain saturation is essential. In particular, we expect these effects to be more important for higher bias currents [1].

ACKNOWLEDGMENTS

We wish to thank Dr. Alex Tikhomirov, Shu Yen Lee, Professor Gerd Leuchs, and Damien Mudge for their thorough and perceptive reading of the manuscript.

[1] K. Petermann, *Laser Diode Modulation and Noise* (Kluwer, Dordrecht, 1988).
[2] S. Tarucha and K. Otsuka, IEEE J. Quantum Electron. **QE-17**, 810 (1981).
[3] M. J. Adams and M. Osinski, IEE Proc., Part I: Solid-State Electron Devices **129**, 271 (1982).
[4] M. Osinski and M. J. Adams, IEE Proc.-J: Optoelectron. **132**, 34 (1985).
[5] L. V. T. Nguyen, M. J. L. Cahill, A. Lowery, D. Novak, P. Gurney, D. D. Sampson, and D.-S. Seo, Opt. Quantum Electron. **28**, 1067 (1996).
[6] L. V. T. Nguyen, A. Lowery, P. Gurney, and D. Novak, Opt. Quantum Electron. **27**, 663 (1995).
[7] D. Marcuse and T. P. Lee, IEEE J. Quantum Electron. **QE-19**, 1397 (1983).
[8] K. Y. Lau, C. Harder, and A. Yariv, IEEE J. Quantum Electron. **QE-20**, 71 (1984).
[9] K. Y. Lau and A. Yariv, in *High-Frequency Current Modulation of Semiconductor Injection Lasers*, edited by W. T. Tsang Semiconductors and Semimetals Vol. 22 (Academic Press, Orlando, 1985), pt. B, p. 69.
[10] K. Petermann, Opt. Quantum Electron. **10**, 233 (1978).
[11] C. H. Henry, in *Spectral Properties of Semiconductor Lasers* (Ref. [9]), pt. B, p. 153.
[12] G. P. Agrawal, Prog. Opt. **XXVI**, 163 (1988).
[13] M. Ito, T. Ito, and T. Kimura, J. Appl. Phys. **50**, 6168 (1979).
[14] G. P. Agrawal, Appl. Phys. Lett. **49**, 1013 (1986).
[15] G. P. Agrawal, IEEE J. Quantum Electron. **26**, 1901 (1990).
[16] E. Hemery, L. Chusseau, and J. Lourtioz, IEEE J. Quantum Electron. **26**, 633 (1990).
[17] L. Chusseau, E. Hemery, and J. Lourtioz, Appl. Phys. Lett. **55**, 822 (1989).
[18] C. H. Lee, T. H. Yoon, and S. Y. Shin, Appl. Phys. Lett. **46**, 95 (1985).
[19] M. Tang and S. Wang, Appl. Phys. Lett. **48**, 900 (1986).
[20] M. Tang and S. Wang, Appl. Phys. Lett. **50**, 1861 (1987).
[21] Y. C. Chen, H. G. Winful, and J. M. Liu, Appl. Phys. Lett. **47**, 208 (1985).
[22] Y. H. Kao, C. H. Tsai, and C. S. Wang, Rev. Sci. Instrum. **63**, 75 (1992).
[23] Y. H. Kao and H. T. Lin, Phys. Rev. A **48**, 2292 (1993).
[24] Y. H. Kao and H. T. Lin, IEEE J. Quantum Electron. **29**, 1617 (1993).
[25] B. K. Goswami, Phys. Lett. A **190**, 279 (1994).
[26] T. H. Yoon, C. H. Lee, and S. Y. Shin, IEEE J. Quantum Electron. **25**, 1993 (1989).
[27] W. Lauterborn and R. Steinhoff, J. Opt. Soc. Am. B **5**, 1097 (1988).
[28] G. Carpintero and H. Lamela, J. Appl. Phys. **82**, 2766 (1997).
[29] S. Bennett, C. M. Snowden, and S. Iezekiel, IEEE J. Quantum Electron. **33**, 2076 (1997).
[30] H. F. Liu and W. F. Ngai, IEEE J. Quantum Electron. **29**, 1668 (1993).
[31] Y. Cho, K. Wada, Y. Akage, K. Ishihara, and H. Horinaka (unpublished).
[32] J. Sacher, D. Baums, P. Panknin, W. Elsässer, and E. O. Gobel, Phys. Rev. A **45**, 1893 (1992).
[33] W. Chow, S. W. Koch, and M. Sargent III, *Semiconductor Laser Physics* (Springer-Verlag, Berlin, 1994).
[34] K. Petermann, IEEE J. Quantum Electron. **QE-15**, 566 (1979).
[35] Y. Suematsu and K. Furuya, Trans. IECE Jpn **60**, 467 (1977).
[36] P. S. Spencer and K. A. Shore, Quantum Semiclassic. Opt. **9**, 819 (1997).
[37] U. Parlitz and W. Lauterborn, Z. Naturforsch. Teil A **41a**, 605 (1986).
[38] K. Wiesenfeld, Phys. Rev. A **32**, 1744 (1985).
[39] C. Scheffczyk, U. Parlitz, T. Kurz, W. Knop, and W. Lauterborn, Phys. Rev. A **43**, 6495 (1991).
[40] B. W. Hakki and T. L. Paoli, J. Appl. Phys. **46**, 1299 (1975).
[41] A. Yariv, *Optical Electronics*, 4th ed. (Saunders College Publishers, Fort Worth, TX, 1991).
[42] R. Olshansky, C. B. Su, J. Manning, and W. Powazinik, IEEE J. Quantum Electron. **QE-20**, 838 (1984).
[43] M. Osinski and J. Buus, IEEE J. Quantum Electron. **QE-23**, 9 (1987).